NIPPON STEEL & SUMITOMO METAL TECHNICAL REPORT No. 117 DECEMBER 2017

Technical Report

UDC 669 . 665 : 548 . 55 : 681 . 3

Computational Materials Science for Developing Sophisticated Top Seeded Solution Growth (TSSG) Processes of Single Crystalline SiC

Koji MORIGUCHI*
Hiroshi KAIDO
Kazuhiko KUSUNOKI
Kazuhito KAMEI
Nobuhiro OKADA
Yutaka KISHIDA
Kazuaki SEKI

Abstract

A solution growth method is a technique in which carbon is dissolved for oversaturation in a solution that consists mainly of silicon. This is followed by taking a SiC single crystal from the liquid phase in the dual phase region in the corresponding phase equilibrium diagram. The potential ability of solution methods has recently attracted attention as sophisticated single crystal growth technology that complements the sublimation method. In this article, using a wide variety of computational materials science along with the remarkable recent progress, we review our theoretical research activities on some issues for developing sophisticated solution growth processes of single crystalline SiC, including the topics of (i) total energetics of nonequivalent hexagonal polytypes for wide-gap semiconductors, (ii) compositional design in solutions based on the CALPHAD (Computer Coupling of Phase Diagrams and Thermochemistry) method, (iii) fluid dynamics analyses coupled with the CALPHAD for designing the growth furnace, and (iv) dislocation dynamics during SiC single crystal growth.

1. Preface

Since the properties of silicon (Si) are now approaching their limits of use for high-performance power devices, silicon carbide (SiC) has been drawing attention as a promising material. Nippon Steel & Sumitomo Metal Corporation has engaged in SiC single crystal development since the beginning of the 1990s. When achieved, SiC power devices are expected to outstrip Si power devices in performance with ten-fold operation frequency, one-hundredth power loss, and three-fold operable temperature range.[1)]

SiC single crystals are normally grown from the gas phase by the sublimation method. The solution method involves dissolving carbon (C) for supersaturation in a solution composed mainly of Si, then pulling out a SiC single crystal from the liquid phase onto the seed crystal in the dual phase region (SiC and liquid phases) in the corresponding phase equilibrium diagram. The method allows the crystal growing process not only at low temperatures, but also under the conditions close to thermal equilibrium, which makes it possible to obtain high quality crystals. Given these advantages, the solution method has been attracting attention recently as single crystal growth technology that complements the sublimation method.[2–5)]

SiC shows various polymorphous structures that differ only in the one-dimensional direction (c-axis one) called polytypes. Polytypes are energetically degenerated with energy of about $\Delta T=2K$ corrected for temperature,[6)] making it difficult to control the phase stability during the crystal growth to obtain a SiC single crystal with the desired polytype. In addition, the growth of a SiC single crystal taking place under high temperature also makes it even more challenging to obtain a good quality single crystal with less disloca-

---

* Chief Researcher, Dr. Eng., Mathematical Science & Technology Research Lab., Advanced Technology Research Laboratories
20-1 Shintomi, Futtsu City, Chiba Pref. 293-8511

tions and stacking faults.[2,3] For this reason, a variety of physical perspectives are being investigated in order to establish better single crystal growing techniques.[4,5]

Meanwhile, computational materials science collectively refers to theoretical simulation technologies for phenomena related to materials and their production processes. Along with the remarkable progress of hardware and software technologies, it is now an essential R&D tool in various engineering fields.[7–9] One of the most important missions of computational materials science is to reproduce realistic material phenomena in computers based on the basic laws of physics (fundamentals and principles), and to analyze the behavior under a particular set of conditions and/or various space and time scales, thereby creating new universal laws and processing conditions. This paper outlines research activities involving the computational materials science conducted by Nippon Steel & Sumitomo Metal for facilitating the sophistication of SiC single crystal growth technology using the solution method.

2. Static Energetics of Nonequivalent Polytypes in Wide-Bandgap Semiconductors

The phase stability in polytypes of Group IV wide-bandgap semiconductors (C, Si, SiC) and Group III-V wide-bandgap semiconductors (BN, AlN, GaN, InN) is extremely important for controlling the formation of a polytype with a desired electronic structure. This chapter reports the results of systematic investigation on the static structural energetics for diverse nonequivalent polytypes exceeding 6 million through analyses coupled with three theoretical calculation tools (PGA: polytype generation algorithm; FPC-DFT: first-principles calculations based on the density functional theory; and ANNNI: axial next-nearest-neighbor Ising model).[6]

2.1 Polytypes and electronic properties

The three-dimensional structure in a SiC crystal is composed of stacked silicon-carbon bilayers as shown in **Fig. 1**(a). During the process, a geometric difference can occur in the positional relationship between upper and lower bilayers, leading to a crystal structure with different unit cell size, different symmetry, and different number of layer units. Such a geometric difference observed in layered substances is called polytypism. In addition, a polymorphic structure in a crystal that differs only in the stacking sequence is called a polytype. While the polytypes made of carbon[10], AlN[11], and, GaN[12], which are wide-bandgap semiconductors, are often experimentally observed, SiC particularly shows several hundred polytypes.[13] The long period stacking ordered (LPSO) Mg alloys with lighter weight, higher specific strength, and higher heat resistance than those in super duralumin are also recently drawing attention, as metallic structural material with similar polytypism to that in SiC.[14]

Figure 1(b) shows typical notations of polytypes. The Ramsdell notation shows the number of stacking periods (L) in a hexagonal unit cell added with the indication of the type of crystal symmetry (H: hexagonal, C: cubic, R: rhombohedral). Since the Ramsdell notation allows distinguishing the stacking periodicity in the c-axis direction in a hexagonal unit cell, it is often used in the same way as 4H-SiC and 6H-SiC. However, a disadvantage is that the notation cannot separately characterize nonequivalent polytypes (Fig. 1(a)) with stacking sequences of L being six or more.

In a hexagonal close-packed stacking structure, there are three different layers often denoted by A, B, and C, corresponding to different atomistic positions in the planes perpendicular to the stacking direction (c-axis). The ABC notation arrays these symbols of layer types to describe the stacking sequence. For example, 2H is described as (AB), while 3C is described as (ABC). For simple close-packed lattices, 2H corresponds to hcp (hexagonal close-packed), while 3C corresponds to face-centered cubic (fcc). Two types of cyclic stacking orders can exist for the ABC notation: A → B → C → A → … (repetition of forward rotation) and A → C → B → A→ … (repetition of backward rotation). A notation that makes the former correspond to "+(Up-spin)" and the latter correspond to "–(Down-spin)" is called the Hägg notation.[15] Since it is consistent with the Ising model composed of lattice points with two possible states, the Hägg notation is often adopted for considering the energetics in polytype structure.[6]

A hcp structure has the stacking sequence of (AB) (AB) (AB)…, while a fcc structure in the cubic crystal system has the (ABC) (ABC)… sequence. When focusing on a layer denoted as X, both

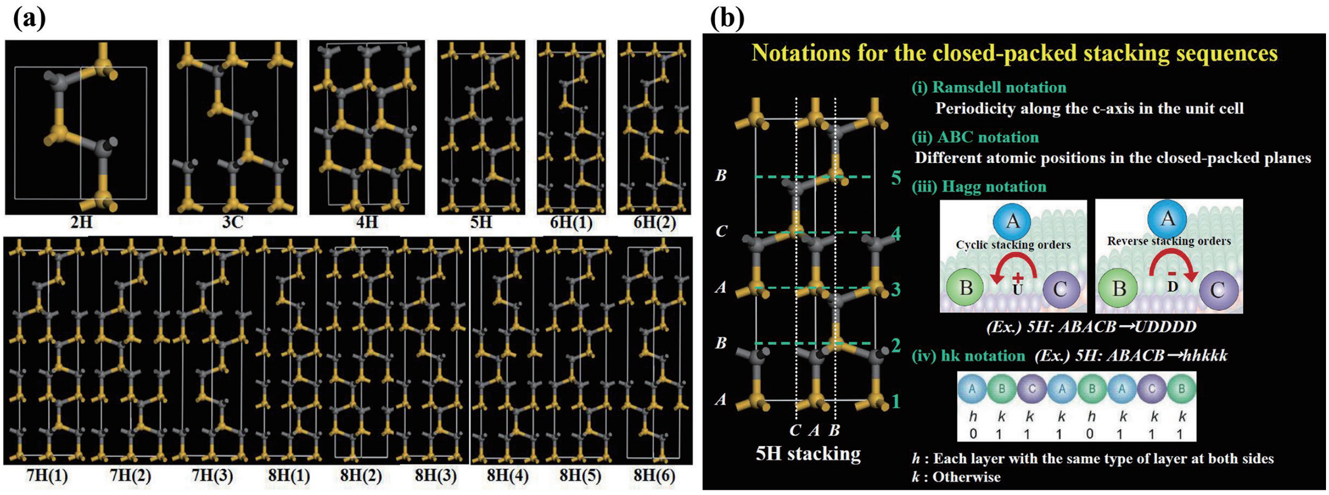

Fig. 1 **(a) Schematic illustration of constructing nonequivalent stacking polytypes with up to the periodic stacking length of $L=8$**
(b) Polytype notations commonly used
Polytypes are characterized by a stacking sequence with a given repeat unit along the hexagonal c-axis direction. Three different layers are often denoted by A, B, and C, corresponding to different atomistic positions in the planes perpendicular to the stacking direction. These descriptions for nearest neighbor stacking result in the so called hk notation.[16] Another notation commonly used in the representation of stacking sequences is the Hägg notation.[15]

sides of X in a hcp structure are found to be of the same layer type (e.g., AXA, BXB, CXC), while in a fcc structure both sides of X are of different layer types (e.g., AXC, BXA, CXB). There is yet another notation that involves making layer X in a hcp structure correspond to letter "h" (from hexagonal) as a layer in a hexagonal crystal system environment, and making layer X in a fcc structure correspond to "k" (from kubik, German translation of cubic) as a layer in the cubic crystal system environment. The notation is called the hk notation.[16] For example, layers of 5H, which can be (ABACB) as shown in Fig. 1 (b), are described as (hhkkk) using the hk notation. The geometric quantity defined by $\sigma_H \equiv n_h/(n_h+n_k)$, where (n_h) is the number of "h" layers in a period in a hexagonal crystal system environment, while (n_k) is the number of "k" layers in a period in a cubic crystal system environment, is called hexagonality. Hexagonality is often a very important parameter when considering the physical properties of a polytype.

Figure 2 shows an example of a crystal grown under the top-seeded solution growth (TSSG) method using a 4H-SiC seed crystal[4, 17] with polytype inclusion during the growth. The figure also shows a graph on which optical band-gap measurement values obtained in the past with respect to typical SiC polytypes are replotted using the data shown in Table II in reference 18). The electronic structure of GaN and other Group III-V nitrides used for LEDs exhibits relative insensitivity which affects device properties, even if there are dislocation defects or stacking faults at high density in the device active layer.[19, 20]

Meanwhile, as shown in the graph of Fig. 2 (c), strong dependency of SiC band-gap on hexagonality is observed.[18] This suggests the possibility of significant change in the electronic structure caused by dislocation defects and stacking faults in the device active layer. In addition, there are reports of several experimental and theoretical studies that a possible driving force can exist for the formation of the above defects capable of altering the electronic structure under the heat and electric field during the production or operation of the device, which results in the emergence of these defects by such heat and electric field during the studies.[21–23] As described above, not only the control of the dislocation defect and stacking fault formation, but also the development of technologies for stably growing crystals with desired polytypes and the control of structural stability in the materials of the substrate under the device operation are important issues to be solved toward the practical use of SiC single crystals as power device materials.

2.2 Total energy analysis method for polytypes using the ANNNI model

The ANNNI model is a kind of Ising model that considers only interlayer interaction in a polytype in the uniaxial direction, and approximates the total energy of the polytype using the following equation,[6, 24]

$$E_{total} = E_0 - \frac{1}{L}\sum_{i=1}^{L}\sum_{n=1}^{\infty} J_n \sigma_i \sigma_{i+n} \tag{1}$$

where L is the periods in the c-axis direction in the polytype, E_0 is the self-energy of the layer, and J_n is the interlayer interaction. For Ising spin σ_i, the Hägg notation described in Section 2.1 is used. The ANNNI model sometimes shows poor convergence of physical quantities considered for a system with significant Friedel oscillation observed in metal systems.[25, 26] In the case of the total energy of a polytype of Group IV and Group III-V wide band-gap semiconductors analyzed here, long-distance interlayer interaction is small, and so the ANNNI model considering up to the third-neighbor layers is often used.[24, 27–30]

Given this, we have also deduced E_0 and J_n from the following project operation,[6]

$$\begin{pmatrix} E_0 \\ J_1 \\ J_2 \\ J_3 \end{pmatrix} = \frac{1}{4}\begin{pmatrix} 1 & 1 & 2 & 0 \\ 2 & -1 & 2 & -3 \\ -1 & -1 & 2 & 0 \\ 0 & -1 & -2 & 3 \end{pmatrix}\begin{pmatrix} E_{2H} \\ E_{3C} \\ E_{4H} \\ E_{6H(2)} \end{pmatrix} \tag{2}$$

where each of E_{2H}, E_{3C}, E_{4H}, and $E_{6H(2)}$ is the total energy of 2H, 3C,

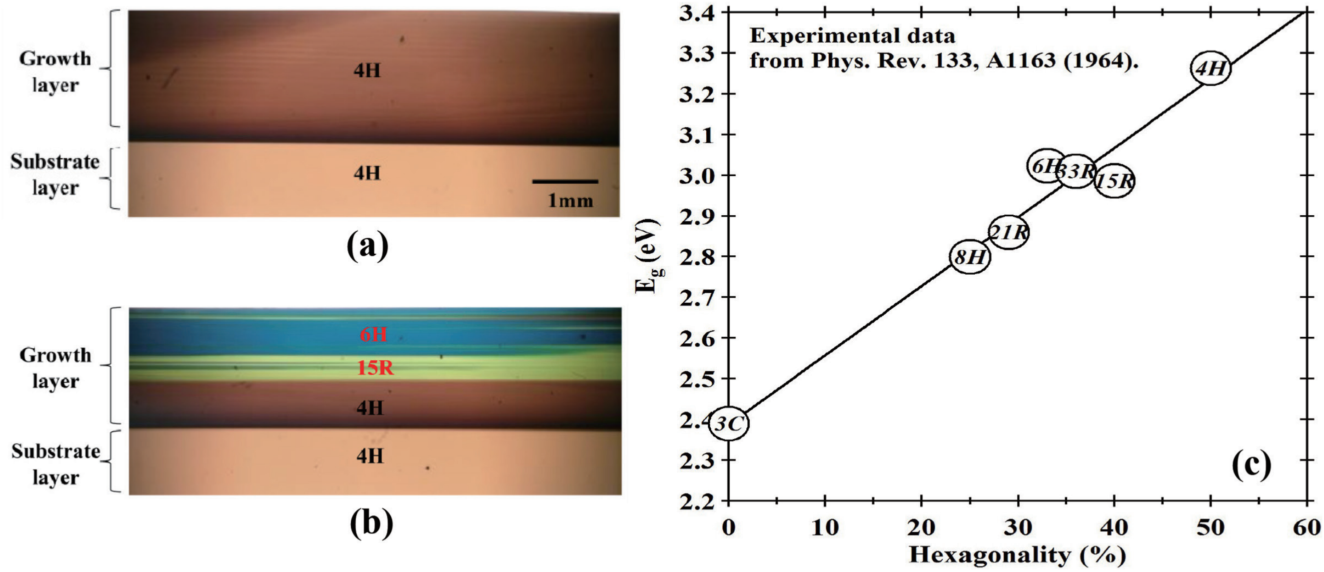

Fig. 2 Typical optical microscope images for polytype inclusions during top seeded solution growth (TSSG) of 4H-SiC
(a) Stable epitaxial growth with polytype stability, (b) Unstable growth with polytype inclusions of 6H and 15R, (c) A plot of band-gaps as a function of "Hexagonality" for seven SiC polytypes
The experimental values listed in Table II in Ref. 18) are used.

4H, and 6H(2) polytypes, respectively, based on the present first-principles calculations. From our analysis, it is estimated that each maximum error distribution of the total energy of the ANNNI model polytype obtained from the projection is about 0.7, 1.3, 2.7, 0.3, 2.9, 1.1 and, 1.2% for C, Si, SiC, BN, AlN, GaN, and InN, respectively.[6)]

Meanwhile, since the number of nonequivalent polytypes increases exponentially for a given period, the methodology to efficiently form a polytype (PGA touched on above) has been handled mainly by researchers in the fields of crystallography and mathematics.[31)] In theoretical studies using first-principles calculations (FPC) and the ANNNI model, calculations have typically been performed for the discrete model systems in which stacking structures are chosen as observed in experiments and correlations between physical properties (such as total energetics and electronic structure etc.) and hexagonality have been discussed in many cases.[24, 27–30)] Since the use of PGA allows efficient examination of polytypes of mathematically-nonequivalent close-packed structures, the correlations between a wider variety of polytype structures and total energy can be deciphered in detail. Based on this concept, the next section describes the results of systematic investigations on the static structural energetics of nonequivalent polytypes using three theoretical tools of PGA, FPC-DFT, and ANNNI.

2.3 Static energetics of polytypes

Through the present first-principles calculations (GGA, plane wave expansion, and ultrasoft pseudopotentials), the structures of all 15 nonequivalent stacking structures from 2H to 8H are energetically optimized. Part of the calculation results was projected to the ANNNI model considering up to the third-neighbor layers as described in Section 2.2 to derive the total energy of each nonequivalent stacking structure with the number of stacking periods L up to 30 (6 209 704 types × seven compounds). Here, the correlations between hexagonality of the system, crystal lattice constant, and the total energy is mainly discussed.

Figure 3(a) shows the relationship between hexagonality (σ_H) and non-dimensional interlayer distance $c/(na)$, which has the ideal value of $\sqrt{2/3}=0.8165$ in 3C, in each compound system. Systems with strong covalency show a linear positive correlation with an increase of σ_H, while systems with strong iconicity show a linear negative correlation with the same. Such linear correlations between σ_H and the crystal structure constant can be found with respect to in-plane lattice constant (a), interlayer lattice constant (c), and equilibrium atomic volume (V_0). (However, the correlation between σ_H and V_0 in Si and SiC systems is weak.)[6)] Figure 3(b) shows the correlation between the GGA-calculated 2H-3C energy difference and the slope constants in Fig. 3(a). It shows very strong linearity for a wide range of compound systems of both ionic and covalent, indicating that the distribution of polytype total energy has a strong correlation with the crystal structure constant's sensitivity to the change in σ_H.

By projecting the first-principles calculation results to the ANNNI model, a polytype energy map with respect to σ_H as shown in **Fig. 4** can be obtained through simple calculations. Figure 4(a) shows an example in a SiC system, while Fig. 4(b) shows all wide-bandgap compound semiconductor systems mapped. All of the systems have the polytype energy range somewhere within the triangle region formed by 3C, 4H, and 2H. In strongly covalent systems, the stacking of 3C ($\sigma_H=0$) is the ground state. In strongly ionic systems, the stacking of 2H ($\sigma_H=1$) is the ground state. Furthermore, it should be noted that the energy distribution region for the polytypes in Fig. 4(b) systematically rotate clockwise around the origin ($\sigma_H=0$) with changing from the strong covalency systems to strong ionicity ones.

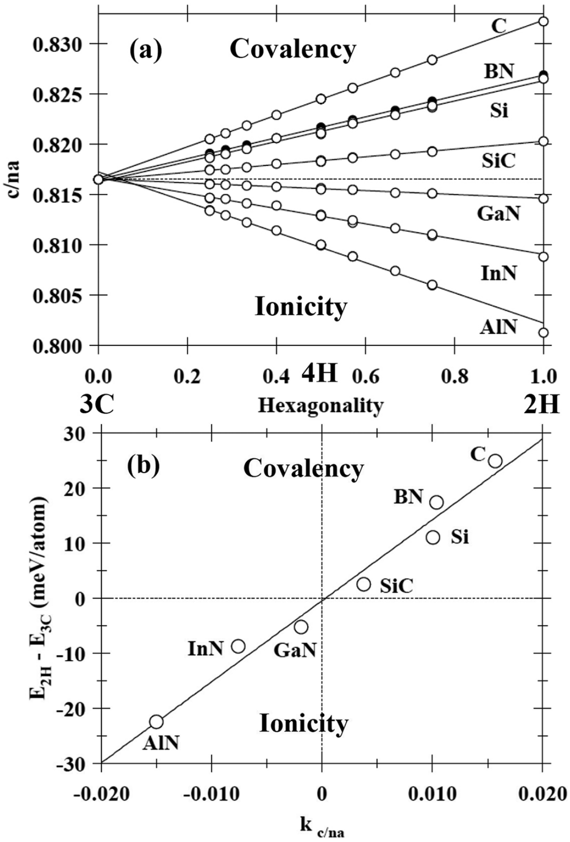

Fig. 3 (a) Optimized ratio $c/(na)$ as a function of hexagonality for C, Si, SiC, and III-V nitrides within the present first-principles (FP) calculations
(b) Correlation between the FP-calculated 2H-3C energy difference and the slope constants of $k(c/(na))$

It is interesting to find a visible critical point of energy at $\sigma_H=0.5$ (4H layers) in a system with strong covalency. Therefore, the energies of the polytypes with hexagonality from $0 \leq \sigma_H \leq 0.5$ are almost degenerated for the SiC system with an intermediate characteristic between covalency and ionicity. However, we have also found that most polytypes with the lowest energy calculated in each periodicity L have been experimentally observed and determined to date.[6)] This fact indicates that the thermodynamic stability is still one of the important factors in selecting the polytypic structures with a given stacking length, although the energy differences of polytypes are generally quite small in the SiC system.

To date, 4H, 6H (6H(2) in this paper), and 15R SiC polytypes have often been observed during crystal growth experiments (Fig. 2). Which polytype is in the ground state has often been a subject under discussion during researches through first-principles calculations.[29, 32)]. The differences between these polytypes in total energy have reached the accuracy limit of first-principles calculations (Fig. 4(a)).[6, 29, 32)] This suggests that we may encounter difficulties never experienced by humans in terms of the phase stability control for the SiC single crystal growth as a wide-bandgap semiconductor production technology.

3. Thermodynamic Properties and Reaction in the Crucible of the Solvent: Analysis Using the CALPHAD Method

For the stable SiC crystal growth under the solution method, it is

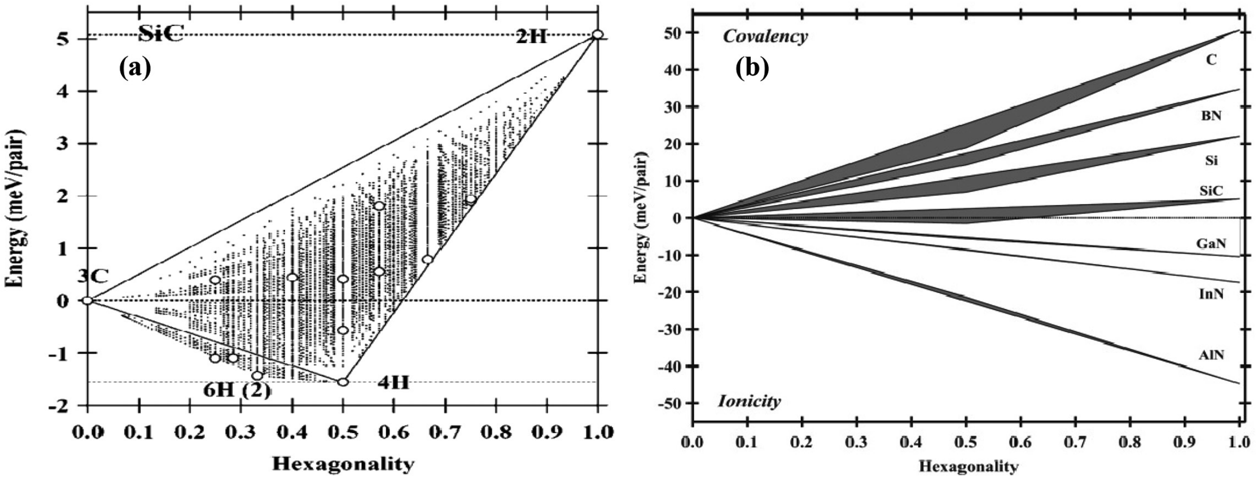

Fig. 4 ANNNI total energies of the non-equivalent polytypes for (a) SiC and (b) All materials considered are plotted as a function of hexagonality Energy is measured from that in the 3C stacking configuration.

important to know thermodynamic physical properties, the reaction path in the crucible, and the reaction driving force of the solvent in order to design the crystal growth furnace and others involved in the process. Using the results of a CALPHAD method analysis,[9] this chapter explains the basic thermodynamic equilibrium physical properties of Cr-Si and Ti-Si solvents[4] used for growing crystals in solutions and their difference.[33] Furthermore, as an example of information that can be obtained through unsteady three-dimensional fluid-thermal coupled analysis combined with the CALPHAD method, we demonstrate the usefulness of computationally visualizing the driving force for the SiC precipitation in the crucible and show that the combined method may be capable of providing new insight useful for the process design including crystal growth furnace design.[33]

3.1 Calculated phase diagrams and reaction paths of Cr-Si and Ti-Si solvents

Figure 5 shows phase diagrams of Cr-Si-C and Ti-Si-C solutions calculated using the SSOL4 thermodynamic database.[34] For the equilibrium calculation, the TQ-interface library[35] is used. However, the quantitative accuracy provided by the SSOL4 database for the phase diagrams is not sufficient, as reported in a recent study that finds a significant overestimation in carbon solubility by the SSOL4 database.[36]

The primary purpose of the addition of Cr and Ti to the solvent was to increase the carbon solubility in the temperature range in which SiC crystals grow. The liquid phase regions of both elements

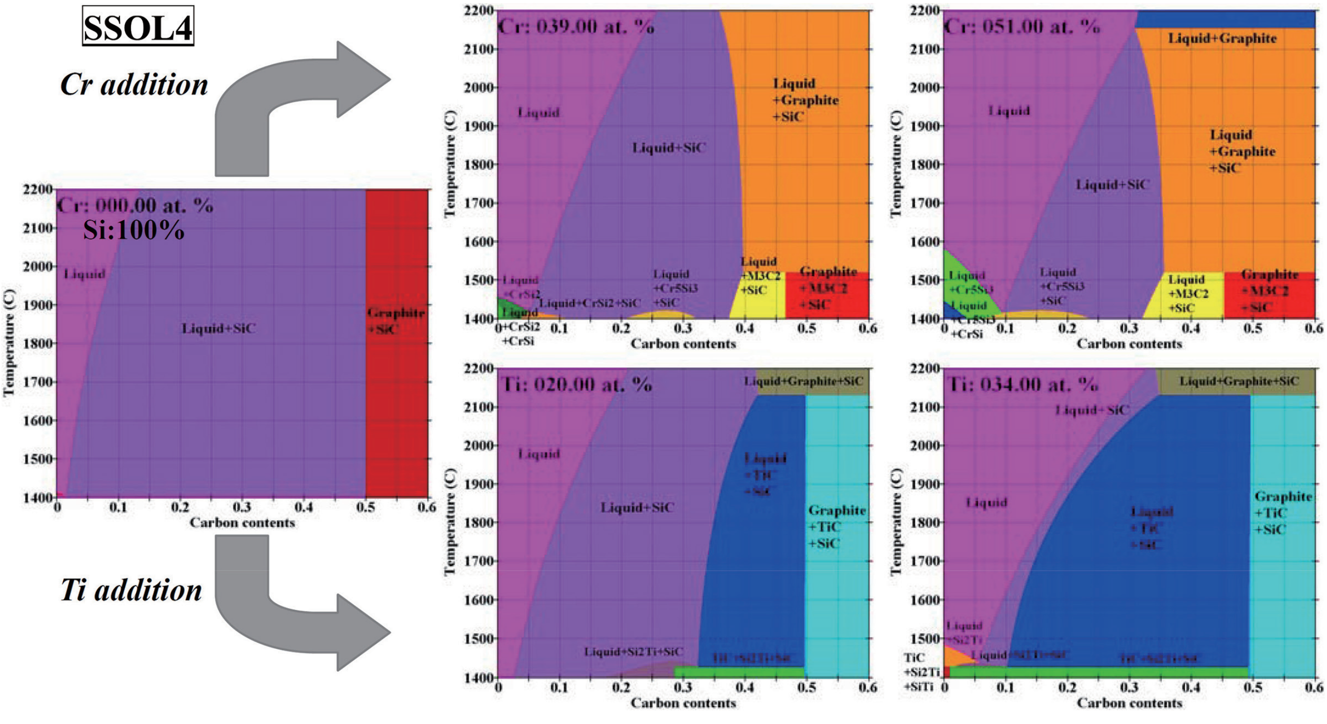

Fig. 5 Calculated phase diagrams as a function of Cr (upper panels) or Ti addition (lower panels) based on the SSOL4 thermodynamic database

increase in the phase diagrams along with the increase in the added amount. However, regarding the solvent with Cr, the dual-phase region consisting of liquid and graphite phases moves toward the lower temperature side along with the increase in the Cr concentration, suggesting the possibility that the primary crystal reaction could change into graphite precipitation in the temperature range of SiC crystal growth. Regarding the solvent with Ti, along with the increase in the Ti concentration, the triphasic range consisting of liquid, SiC, and TiC phases extend from the side of high carbon concentration. The triphasic range crosses the solubility curve at a Ti concentration where the primary crystal reaction changes into TiC precipitation. In fact, for solvents with Cr with which a certain level of prolonged thick film growth is succeeded, a significant change in the solution composition has been observed. In addition, the primary crystal change reaction described above has been experimentally confirmed.[4, 33] This suggests that some sort of improvement measures, such as those for the raw material supply, are required for crystal growing furnaces that are likely to cause a significant change in solution composition.

3.2 SiC precipitation reaction driving force in various solutions

In a study under the Wilson-Frenkel approximation framework that considered the growth rate is linearly proportional to the reaction driving force,[37] understanding the actual reaction driving force is important. The CALPHAD method, which uses Gibbs free energy for the basic database, can easily calculate the driving force for the SiC precipitation in various super-saturated solutions. **Figure 6** shows contour maps[33] of the SiC precipitation driving force in solution systems that we often use. Contrary to the solution system of 100% Si (Fig. 6(a)), in each of Ti- (Fig. 6(b)) and Cr- (Fig. 6(c)) containing solutions, an increase of the reaction driving force is observed at the same carbon super-saturation level. In particular, in that of Cr-containing, the driving force in the high super-saturation region is markedly increased, showing superiority in high-speed crystal growing of Cr-containing solutions. Furthermore, all solutions in Fig. 6 show driving force contours going down along the temperature scale toward higher temperatures. Given the driving force behavior, as the growing temperature increases, a higher growing rate is anticipated at the same super-saturation level. Understanding the reaction driving force like this can be useful as well for considerations on the differences in the occurrence of undesired crystals and nucleation phenomenon brought by difference in the solution type.[4)]

3.3 Combining fluid-thermal coupled analysis and the CALPHAD method

Whereas understanding the reaction driving force is useful for the comprehension of various reactions in the crucible, it is difficult to directly observe the temperature or carbon super-saturation distribution necessary for the calculations. Given this, an effective method is combining the fluid-thermal coupled analysis and the CALPHAD method.[33] If the SiC single crystal growth furnace is heated by high frequency induction during the crystal growth under the solution method, Lorentz force is generated in the solution, significantly affecting the solution flow. In order to ensure the crystal growth rate and its uniformity during the crystal growth using the solution method, it is necessary to appropriately control the temperature distribution and flow distribution of the solution. Since direct measurement of the flow rate and temperature distribution of the solution under a high temperature is likely to be difficult, analysis using a numerical model becomes helpful. We have developed a fluid-thermal coupled analysis model of unsteady three-dimensional analysis that handles the liquid and gas flow in the crystal growing furnace and adopted the furnace.[4, 38, 39]

The distribution of Joule's heat and Lorentz force during high frequency induction heating is calculated using the three-dimensional finite element method with side elements.[40] Using the calculated distributions, the fluid-thermal coupled phenomena are analyzed. The governing equations of the thermos-hydraulic analysis are shown below,

$$\nabla\cdot\mathbf{u} = 0 \tag{3}$$

$$\frac{\partial\mathbf{u}}{\partial t} = -\nabla\cdot(\mathbf{uu}) - \frac{\nabla p}{\rho} - \frac{1}{\rho}\nabla\cdot(\mu\nabla\mathbf{u}) - \beta(T-T_0)\mathbf{g} + \mathbf{F} \tag{4}$$

$$\frac{\partial T}{\partial t} = -\nabla\cdot(\mathbf{u}T) + \frac{1}{\rho C_p}\nabla\cdot\lambda\nabla T + Q \tag{5}$$

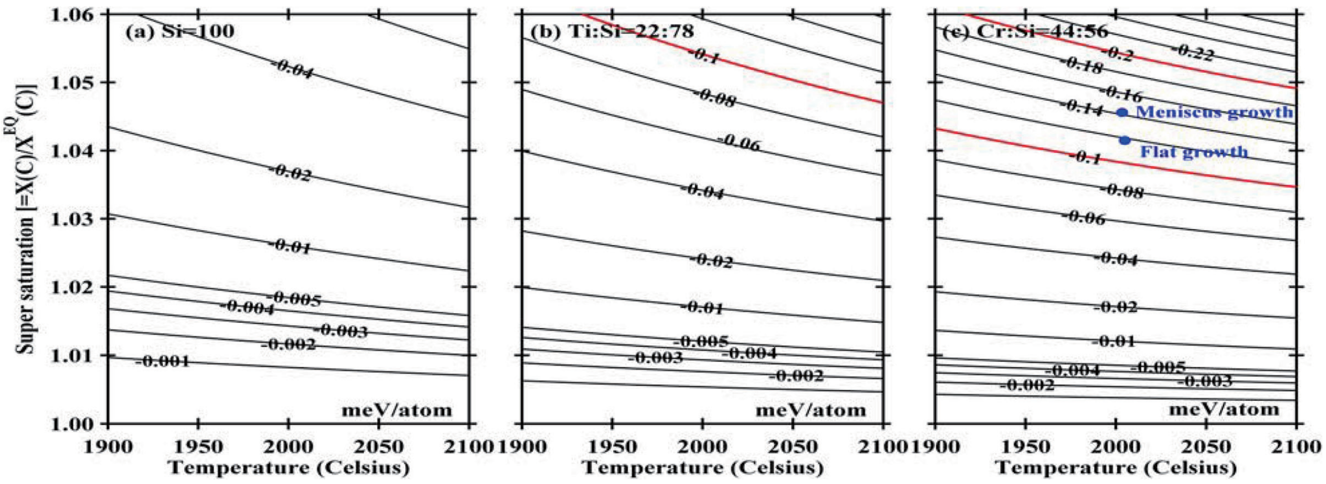

Fig. 6 Contour maps of driving forces (in meV/atom) for SiC precipitate as a function of temperature and carbon super-saturation in (a) Si=100, (b) Ti : Si=22 : 78, and (c) Cr : Si=44 : 56 solutions
We have also plotted the positions of driving force at the solid/liquid interface during the flat and meniscus growth modes based on the computational analyses depicted in Fig. 7(c). All calculations are performed based on the SSOL4 thermodynamic database.

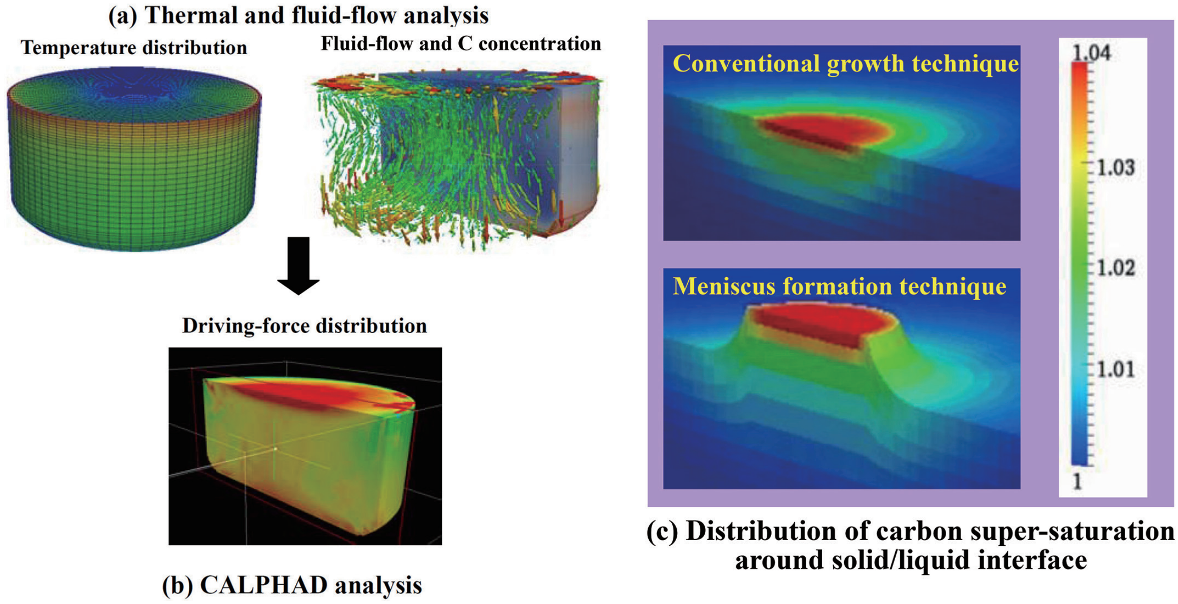

Fig. 7 (a), (b) CALPHAD analyses for driving-force distribution in growth crucibles assisted by three dimensional non-steady-state thermal and fluid-flow simulations
(c) Distribution of carbon super-saturation around solid/liquid interface simulated for the conventional growth mode (upper panel) and meniscus one (lower panel)

$$\frac{\partial C}{\partial t} = -\nabla \cdot (\mathbf{u}C) + \nabla \cdot D \nabla C + C_{react} \qquad (6)$$

$$C_{react} = -A_0 (C - C_e) \exp\left(\frac{-E_0}{RT}\right) \qquad (7)$$

$$C_e = 4.433 \times 10^{-3} (T - 1687)^2 \qquad (8)$$

where **u** is the flow rate, μ is viscosity coefficient, ρ is specific gravity, p is pressure, β is the volume expansion rate, T_0 is average temperature of the solution, **g** is gravitational acceleration, **F** is Lorentz force density vector, C_p is specific heat, T is temperature, λ is thermal conductivity, Q is Joule heat density, C is dissolved carbon concentration, D is diffusion coefficient of carbon, C_{react} is crystal growth rate, C_e is carbon solubility, E_0 is activation energy, A_0 is growth rate constant, and R is gas constant.

The numerical calculations are performed with the large eddy simulation (LES) model applied to the turbulence model,[41] the central difference applied to the advection term of the momentum, and a third-order upwind difference scheme and total variation diminishing (TVD)[42] applied to other transport equations. Equation (7), which is the Wilson-Frenkel model touched on the previous section, is often used for consideration of the crystal growth speed under process conditions. For the carbon solubility responsible for local equilibrium on the crucible wall, Eq. (8) is used in a approximative manner.[43] More detailed numerical calculation methods and physical property values adopted are described in reference 39).

The use of the numerical calculation results of the unsteady three-dimensional fluid-thermal coupled analysis described above as the information entered into the CALPHAD method allows acquiring knowledge on spatiotemporal fluctuation of the driving force in the crucible, and thus allowing qualitative estimation of the precipitation reaction sites and reaction rate in various solution compositions (**Fig. 7**(a) and 7(b)). To suppress the formation of undesired crystals around the crystal holding shaft, we have proposed a meniscus forming method[4] that involves bringing the seed crystal into contact with the solution surface, and then pulling the seed crystal up approx. 0.2 mm to 1.0 mm to form the meniscus during the crystal growing process, as shown in the lower image of Fig. 7(c). Figure 7(c) also shows the change in carbon saturation distribution in the vicinity of the growth interface during the crystal growth both using a conventional solution method and using the method with the meniscus. In addition, Fig. 6(c) shows the driving force positions of both methods in the case where a Cr-containing solvent is used estimated from the analysis explained in this section. The analysis results suggest the possibility that the meniscus formation brings about an increase in the SiC precipitation driving force.[4, 33] The fluctuation of the carbon super-saturation level is considered to constitute the cause of unstable surface morphology. For this reason, keeping the meniscus height within an appropriate range during the growing process is an important control principle to obtain a bulk crystal excellent in surface flatness.[4]

4. Consideration on the Dislocation Conversion Behavior in SiC Based on the Theory of Elasticity

Focusing on the dislocation conversion behavior, which leads to a defect density reduction in SiC, this chapter describes the effort to clarify the conversion properties from the theory of elasticity.[44] Defects contained in a SiC crystal are threading edge dislocations (TEDs) extending in the <0001> direction (c-axis direction), threading screw dislocations (TSDs), basal plane dislocations (BPDs) existing on the {0001} plane, stacking faults, etc. As described in Chapter 2, the electronic structures in SiC crystal systems are susceptible to the influence of the microscopic defects, which constitute the major cause of device performance deterioration. For this reason, the defect density reduction is a technical issue.[4] In particular, threading dislocations represented by TEDs or TSDs have an adverse effect on the voltage resistance and oxidation properties of a device.[45] Recently, it has been reported that conversion from TSDs into stacking faults, and from TEDs into BPDs, has occurred during the SiC crystal growing process using the solution method,[46, 47] raising the possibility of growing a high-quality crystal by discharging such defects on the basal plane that have undergone conversion out of the crystal. The conversion behavior of threading dislocations, focusing on that from TEDs to BPDs in particular, is described below.

The conversion behavior from TEDs to BPDs has been reported to include the change in the conversion rate in accordance with the Burgers vector and step flow direction.[47] This finding interestingly suggests that the conversion rate from TEDs to BPDs can be significantly altered by controlling the step flow direction. The following describes an example of attempts to estimate the TED conversion rate from the viewpoint of the dislocation theory and elasticity theory. When dislocations are contained in a crystal, free energy of the crystal increases. The major part of the free energy derives from the elastic energy caused by deflection of the structures in the crystal around individual dislocations.

Figure 8(a) and 8(b) shows the elastic energy distribution around an edge dislocation and a screw dislocation that are considered as linear dislocations of infinite length in the direction vertical to the plane of paper in an infinite solid. The elastic energy is isotropically distributed around the screw dislocation as seen in Fig. 8(b), while the distribution of the edge dislocation is anisotropic as shown in Fig. 8(a). In fact, the elastic energy of an edge dislocation is derived from the following equation based on the linear elastic theory,

$$G^e(r,\theta) = \frac{\mu b^2}{2\pi^2 r^2}\,\frac{(\lambda+\mu)(\lambda\cos^2\theta+\mu)}{(\lambda+2\mu)^2} \tag{9}$$

where r is the distance from the dislocation core, and θ is the angle with Burgers vector $\boldsymbol{b}$. λ and μ are Lame's constants of an isotropic elastic media.

In addition, when the energy gradient (elastic potential) is derived from Eq. (9), the following equation is obtained.

$$\frac{\partial G^e(r,\theta)}{\partial r} = -\frac{\mu b^2}{\pi^2 r^3}\,\frac{(\lambda+\mu)(\lambda\cos^2\theta+\mu)}{(\lambda+2\mu)^2} \tag{10}$$

For comparison on the isoenergy lines in Fig. 8(a), a condition of $G^e(r_1, 0°)=G^e(r_2, \theta)$ is provided, and then anisotropy of the elastic potential expressed by Eq. (10) is obtained as standardized parameter α expressed by the following equation.

$$\alpha(\theta) \equiv \frac{\partial G^e/\partial r\big|_{r=r_2}}{\partial G^e/\partial r\big|_{\substack{r=r_1\\ \theta=0°}}} = \sqrt{\frac{\lambda+\mu}{\lambda\cos^2\theta+\mu}} \tag{11}$$

$\boldsymbol{b}$ of a TED in a hexagonal crystal system has six orientations of 1/3<11-20>. Based on an experimental result[47] showing that almost all of two types of TEDs with $\boldsymbol{b}$ parallel to the step flow direction were converted while the conversion rate of other TEDs was markedly reduced, it is assumed that when θ is 0° or 180°, the conversion rate will be 100%; and when θ is a right angle, the conversion rate will be 0%. According to this assumption, dislocation conversion rate E[%] is expressed by the following equation.

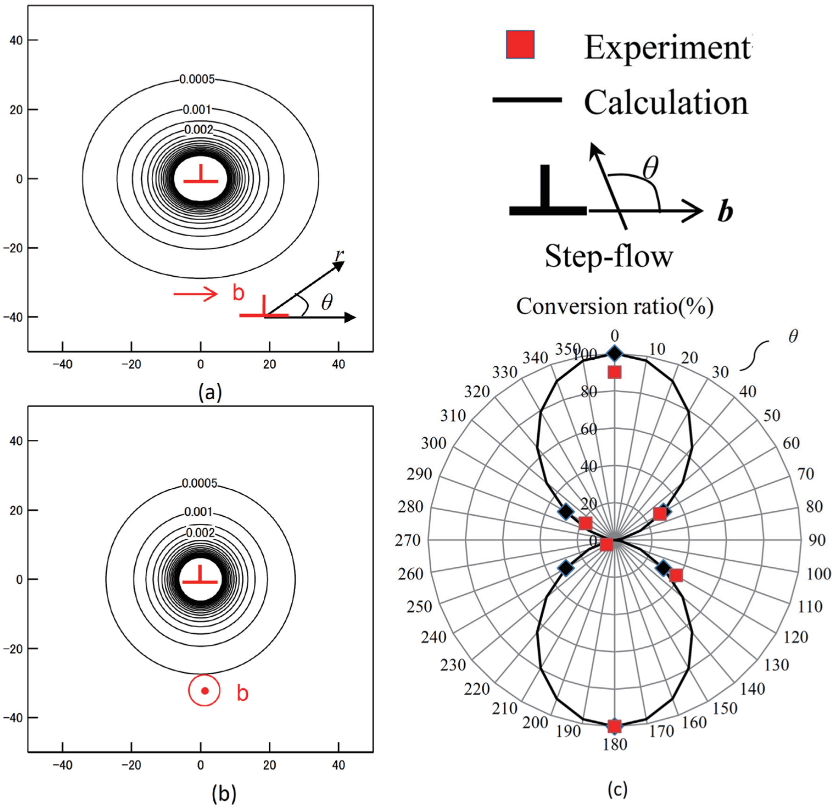

Fig. 8 Elastic energy distribution calculated for (a) edge dislocation and (b) screw one
Unit of axis is set to be Burgers vector *b*. Energy unit is chosen to be $\mu b^2/(4\pi^2(1-\nu))$ and $\mu b^2/8\pi^2$ for edge dislocation and screw one, respectively.
(c) Comparative plots between simulated and experimental[47] conversion ratio of TED

$$E(\theta) \equiv \frac{\alpha(90°)-\alpha(\theta)}{\alpha(90°)-\alpha(0°)} \times 100\,[\%] = \frac{\sqrt{\dfrac{\lambda+\mu}{\mu}} - \sqrt{\dfrac{\lambda+\mu}{\lambda\cos^2\theta+\mu}}}{\sqrt{\dfrac{\lambda+\mu}{\mu}}-1} \times 100\,[\%] \tag{12}$$

Figure 8 (c) shows a comparative chart between the conversion rate obtained using Eq. (12) and experimental results.[47] As seen from the figure, the TED conversion rate estimation formula above replicates the tendency of the experimental results. Equation (12) can estimate the conversion rate for any θ not examined in the experiments as well.

Next, an examination considering the actual step flow conditions is described. **Figure 9** shows a schematic view of the positional relationship between TEDs and the step flow direction assumed for this examination. In this analysis, it is assumed that TEDs with six different Burgers vectors are uniformly distributed. For discussion on the actual dislocation conversion rate, the average conversion rate is important. The average conversion rate is defined by the following equation as the arithmetic mean of the TEDs' conversion rates.

$$E^{average}(\theta) = \frac{E(\theta) + E(60°-\theta) + E(120°-\theta)}{3} \tag{13}$$

The reason for defining the average conversion rate as the average of TEDs with three Burgers vectors is that three out of six Burgers vectors are equivalent in terms of the conversion rate when Eq. (12) is used, despite the only difference in the sign being positive or negative.

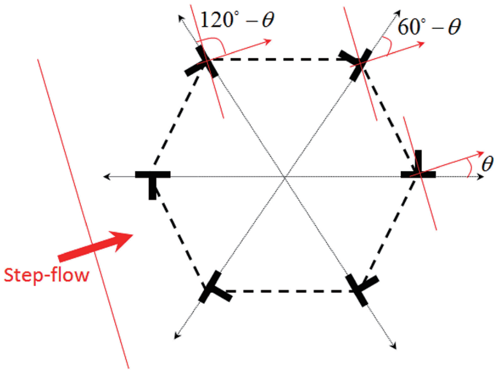

Fig. 9 Schematic illustration of TED distribution with the six types of Burgers vectors along a hypothetically unique directional step flow

Table 1 Simulated dislocation conversion ratio of TED with three types of Burgers vectors
Average conversion ratio defined by Eq. (13) is also listed.

θ	$E(\theta)$	$E(60°-\theta)$	$E(120°-\theta)$	E^{ave} (%)
90°	0.0	79.6	79.6	53.1
80°	3.9	90.7	64.9	53.2
70°	14.8	97.7	47.8	53.4
60°	30.3	100.0	30.3	53.5
50°	47.8	97.7	14.8	53.4
40°	64.9	90.7	3.9	53.2
30°	79.6	79.6	0.0	53.1
20°	90.7	64.9	3.9	53.2
10°	97.7	47.8	14.8	53.4
0°	100.0	30.3	30.3	53.5

Table 1 shows each conversion rate of TEDs with three different Burgers vectors with respect to various θ and the average conversion rate. If θ is varied in the range from 0° to 90°, the conversion rate is changed by no more than about 0.5%. This suggests that the control for the step flow in one direction alone cannot significantly alter the conversion rate. While the actual step flow is not always in one direction, the use of the analysis in this chapter is expected to be helpful in establishing the step flow control principles effective for the adjustment of the conversion rate.

5. Conclusion

As computational materials science research carried out at Nippon Steel & Sumitomo Metal in order to provide support in the sophistication of the SiC single crystal growing technology using the solution method, this paper described (i) energetics of polytypes in wide band-gap semiconductors, (ii) solution design using phase diagram calculations (CALPHAD method), (iii) a method using fluid mechanics and the CALPHAD method in combination for crystal growing furnace design, and (iv) analysis example on dislocation dynamics in a crystal during the growing process. Not only the control of dislocation defects and stacking faults, but also the development of the stable growth technology to obtain the desired polytype and control of structural stability of the substrate material in the device operation constitute major issues to be solved toward the practical use of SiC single crystals as a power device material. Currently, a broad range of approaches is taken in computational materials science. Going forward, by matching the right method with the right location to the extent possible, we would like to continue information provision to contribute to the advancement of Nippon Steel & Sumitomo Metal's SiC single crystal growing technology using the solution method. In concluding this paper, we anticipate the fusion of advanced experimental science and computational science bringing about further development in the advancement of SiC single crystal growing technology.

Acknowledgment

The contents of this technical paper include the results from the joint research with the Higashi-Fuji Technical Center of Toyota Motor Corporation. We extend our deep appreciation to the people who cooperated with us to complete this paper.

References

1) Ohashi, W., Sakamoto, H., Tanaka, M., Fujimoto, T., Dohnomae, H., Morita, M.: Shinnittetsu Giho. (391), 175 (2011)
2) Danno, K.: OYO-BUTSURI. 83 (12), 993 (2014)
3) Kusunoki, K.: Doctoral Dissertation Titled "Study on 4H-SiC Bulk Crystal Growth by Solution Technique and Conduction Type Control." (10725), Nagoya University, 2014
4) Kusunoki, K., Seki, K., Kishida, Y., Moriguchi, K., Kaido, H., Okada, N., Kamei, K.: Development of High Quality 4H-SiC Single Crystal Wafers Grown by Solution Growth Technique. Shinnittetsu Sumikin Giho. (407), 50 (2017)
5) Moriguchi, K., Matsuzaki, Y.: Shinnittetsu Sumikin Giho. (404), 81 (2016)
6) Moriguchi, K., Kamei, K., Kusunoki, K., Yashiro, N., Okada, N.: J. Mater. Res. 28 (1), 7 (2013)
7) Raabe, D.: Computational Materials Science: The Simulation of Materials, Microstructures and Properties. New York, Wiley-VCH, 1998
8) Deák, P., Frauenheim, T., Pederson, M. R.: Computer Simulation of Ma-

terials at Atomic Level. Berlin, Wiley-VCH, 2000
9) Saunders, N., Miodownik, A. P.: CALPHAD (Calculation of Phase Diagrams). A Comprehensive Guide. New York, Pergamon, 1998
10) Lifshitz, Y., Duan, X. F., Shang, N. G., Li, Q., Wan, L., Bello, I., Lee, S. T.: Nature. 412, 404 (2001)
11) Onojima, N., Suda, J., Kimoto, T., Matsunami, H.: Appl. Phys. Lett. 83, 5208 (2003)
12) Selke, H., Kirchner, V., Heinke, H., Einfeldt, S., Ryder, P. L., Hommel, D.: Journal of Crystal Growth. 208, 57 (2000)
13) Jepps, N. W., Page, T. F.: Prog. Cryst. Growth Charact. Mater. 7, 259 (1983)
14) Kawamura, Y., Yamasaki, M.: Materials Transactions. 48, 2986 (2007)
15) Sebastian, M. T., Krishna, P.: Random, Non-Random and Periodic Faulting in Crystals. Amsterdam, Gordon and Breach, 1994
16) Jagodzinski, H.: Acta Crystallogr. 7, 300 (1954)
17) Kamei, K,. Kusunoki, K., Yashiro, N., Okada, N., Tanaka, T., Yauchi, A.: Journal of Crystal Growth. 311 (3), 855 (2009)
18) Choyke, W. J., Hamilton, D. R., Patrick, L.: Phys. Rev. 133, A1163 (1964)
19) Lester, S. D., Ponce, F. A., Craford, M. G., Steigerwald, D. A.: Appl. Phys. Lett. 66, 1249 (1995)
20) Stampfl, C., Van de Walle, C. G.: Phys. Rev. B 57, R15052 (1998)
21) Galeckas, A., Linnros, J., Pirouz, P.: Appl. Phys. Lett. 81, 883 (2002)
22) Galeckas, A., Linnros, J., Pirouz, P.: Phys. Rev. Lett. 96, 025502 (2006)
23) Thomas, T., Pandey, D., Waghmare, U. V.: Phys. Rev. B 77, 121203 (2008)
24) Cheng, C., Needs, R. J., Heine, V.: J. Phys. C 21, 1049 (1988)
25) Bruinsma, R., Zangwill, A.: Phys. Rev. Lett. 55, 214 (1985)
26) Abbasi, A., Dick, A., Hickel, T.: J. Neugebauer, Acta Mater. 59, 3041 (2011)
27) Raffy, C., Furthmüller, J., Bechstedt, F.: Phys. Rev. B 66, 075201 (2002)
28) Kobayashi, K., Komatsu, S.: J. Phys. Soc. Jpn. 77, 084703 (2008); ibid. 78, 044706 (2009)
29) Limpijumnong, S., Lambrecht, W. R. L.: Phys. Rev. B 57, 12017 (1998)
30) Wright, A. F.: J. Appl. Phys. 82, 5259 (1997)
31) Estevez-Rams, E., Martinez-Mojicar, J.: Acta Cryst. A 64, 529 (2008) and References Therein.
32) Bernstein, N., Gotsis, H. J., Papaconstantopoulos, D. A., Mehl, M. J.: Phys. Rev. B 71, 075203 (2005)
33) Moriguchi, K., Okada, N., Kamei, K., Kusunoki, K., Yashiro, N., Oguro, H., Kado, M., Suzuki, H., Sakamoto, H., Bessho, T.: Thermodynamic Properties of Solvents and Chemical Reactions in Crucible for SiC Solution Growth: Computational Analyses Using CALPHAD Method. Proceedings of the 20th Meeting on SiC and Related Wide Bandgap Semiconductors, P-2, 2011
34) Thermo-Calc Database Guide. Thermo-Calc Software AB, Stockholm, 2006
35) Thermodynamic Calculation Interface: TQ-Interface (Version 8.0) Programmer's Guide. Thermo-Calc Software AB, Stockholm, 2013
36) Narumi, T., Kawanishi, S., Yoshikawa, T., Kusunoki, K., Kamei, K., Daikoku, H., Sakamoto, H.: Journal of Crystal Growth. 408, 25 (2014)
37) Saito, Y.: Statistical Physics of Crystal Growth. World Scientific Publishing Co. Pte. Ltd., Singapore, 1996
38) Okada, N., Kamei, K., Kusunoki, K., Yashiro, N., Moriguchi, K., Oguro, H., Kado, M., Suzuki, H., Sakamoto, H., Bessho, T.: 3-Dimensional Numerical Analysis Model of SiC Solution Growth. Proceedings of the 20th Meeting on SiC and Related Wide Bandgap Semiconductors, P-1, 2011
39) Okada, N., Kusunoki, K., Kamei, K., Yashiro, N., Yauchi, A.: Numerical Fluid Flow Analysis during Solution Growth of SiC Crystal using ACRT. The 5th International Symposium on Electromagnetic Processing of Materials. 2006, Sendai, Japan, ISIJ, p. 170
40) Okada, N., Sakamoto, H., Matuo, T., Takatani, K.: Tetsu-to-Hagané. 98 368–377 (2012)
41) Kajishima, T.: Numerical Simulation of Turbulent Flows. Yokendo, Tokyo, 1999
42) Daiguji, H.: Computational Fluid Dynamics. Tokyo, University of Tokyo Press, 1992
43) Kusunoki, K., Munetoh, S., Kamei, K., Hasebe, M., Ujihara, T., Nakajima, K.: Materials Science Forum. 457–460, 123 (2004)
44) Seki, K., Kusunoki, K., Kaido, H., Moriguchi, K., Kamei, K.: The 63rd Japan Society of Applied Physics Spring Meeting. 2016, 20a-H101-5, 2016
45) Otani, N.: Proceedings of 17th Meeting on SiC and Related Wide Bandgap Semiconductors. 2008, p. 8
46) Yamamoto, Y., Harada, S., Seki, K., Horio, A., Mitsuhashi, T., Ujihara, T.: Appl. Phys. Experss. 5, 115501 (2012)
47) Harada, S., Yamamoto, Y., Seki, K., Horio, A., Tagawa, M., Ujihara, T.: Acta Materialia. 81, 284–290 (2014)

Koji MORIGUCHI
Chief Researcher, Dr. Eng.
Mathematical Science & Technology Research Lab.
Advanced Technology Research Laboratories
20-1 Shintomi, Futtsu City, Chiba Pref. 293-8511

Nobuhiro OKADA
Senior Researcher, Dr. Eng.
Mathematical Science & Technology Research Lab.
Advanced Technology Research Laboratories

Hiroshi KAIDO
Researcher
Mathematical Science & Technology Research Lab.
Advanced Technology Research Laboratories

Yutaka KISHIDA
Senior Researcher, Dr. Eng.
Mathematical Science & Technology Research Lab.
Advanced Technology Research Laboratories

Kazuhiko KUSUNOKI
Senior Researcher, Dr. Eng.
Materials Research Lab.
Advanced Technology Research Laboratories

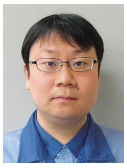

Kazuaki SEKI
Researcher, Dr. Eng.
Materials Research Lab.
Advanced Technology Research Laboratories

Kazuhito KAMEI
General manager, Dr. Eng.
Amagasaki Unit
Nippon Steel & Sumikin Technology Co., Ltd.